**Atmospheric
Chemistry
and Physics**

Characteristics of aerosol and cloud particle size distributions in the tropical tropopause layer measured with optical particle counter and lidar

S. Iwasaki[1], K. Maruyama[2], M. Hayashi[3], S.-Y. Ogino[4], H. Ishimoto[5], Y. Tachibana[4,6], A. Shimizu[7], I. Matsui[7], N. Sugimoto[7], K. Yamashita[3], K. Saga[3], K. Iwamoto[8], Y. Kamiakito[9], A. Chabangborn[10], B. Thana[10], M. Hashizume[10], T. Koike[11], and T. Oki[12]

[1]Department of Earth and Ocean Sciences, National Defense Academy, 1-10-20 Hashirimizu, Yokosuka, Kanagawa 239-8686, Japan
[2]Department of Information and Systems Engineering, Kanazawa University, Kakuma-machi, Kanazawa 920-1192, Japan
[3]Department of Earth System Science, Fukuoka University, 8-19-1 Nanakuma, Jonan, Fukuoka 814-0180, Japan
[4]Institute of Observational Research for Global Change, Japan Agency for Marine-Earth Science and Technology, 2-15 Natsushima, Yokosuka 237-0061, Japan
[5]Meteorological Research Institute, 1-1 Nagamine, Tsukuba, Ibaraki 305-0052, Japan
[6]Graduate School of Earth and Environmental Science, Tokai University, 1117 Kitakaname, Hiratsuka 259-1292, Japan
[7]National Institute for Environmental Studies, 16-2 Onogawa, Tsukuba, Ibaraki 305-8506, Japan
[8]National Research Institute for Earth Science and Disaster Prevention, 3-1 Tennodai, Tsukuba 305-0006, Japan
[9]Graduate School of Science, Tokai University, 1117 Kitakaname, Hiratsuka 259-1292, Japan
[10]Faculty of Science, Chulalongkorn University, 254 Phyathai Road, Patumwan, Bangkok 10330, Thailand
[11]School of Engineering, The University of Tokyo, 7-3-1 Hongo, Bunkyo 113-0033, Japan
[12]Institute of Industrial Science, The University of Tokyo, 4-6-1 Komaba, Meguro 153-8505, Japan

Abstract. An optical particle counter (OPC) is used in conjunction with lidar measurements to examine the characteristics of the particle size distribution in cirrus cloud in the tropical tropopause layer (TTL) over Thailand where the TTL is defined as the height at which temperature is lower than $-75°C$ in this paper. Of 11 OPC launches, cirrus cloud was detected at 10–15 km high on 7 occasions, cirrus was detected in the TTL in 6 cases, and simultaneous OPC and lidar measurements were made on two occasions. Comparison of lidar and OPC measurements reveal that the cloud heights of cirrus in the TTL varies by several hundred meters over distances of tens kilometers; hence the height is not always horizontally uniform. The mode radii of particles constituting the clouds are estimated by lidar and OPC measurements to be less than approximately $10\,\mu m$. The regression lines of the particle size distribution with and without cirrus cloud exhibit similar features at equivalent radii of $<0.8\,\mu m$. Enhancement in the integrated number concentration at radii greater than $0.8\,\mu m$ indicates that liquid particles tend to be frozen at a radius of $0.8\,\mu m$, with cirrus clouds above $10\,km$ exhibiting similar features. On the other hand, enhancement in the particle size distribution at radii greater than $0.9\,\mu m$ and a peak at around $0.8\,\mu m$ in the ratio of the standard deviation of count values to that of the Poisson distribution of the averaged count values are common features of cirrus clouds in the TTL, where the ratio shows the vertical homogeneity of the particle number. These typical features suggest that the transition from liquid, sulfuric acid aerosol, to ice is more observable in the TTL and the timing of freezing may vary with height in the TTL.

1 Introduction

Cirrus cloud in the tropical tropopause layer (TTL; Highwood and Hoskins, 1998), hereafter TTL cloud, generally exists at a height of around $17\,km$ in the TTL, where the TTL cloud includes subvisual cirrus clouds (SVCs) which are defined as cirrus with an optical thickness less than 0.03 (Sassen and Cho, 1992). Using data obtained in the second

Correspondence to: S. Iwasaki
(iwasaki@nda.ac.jp)
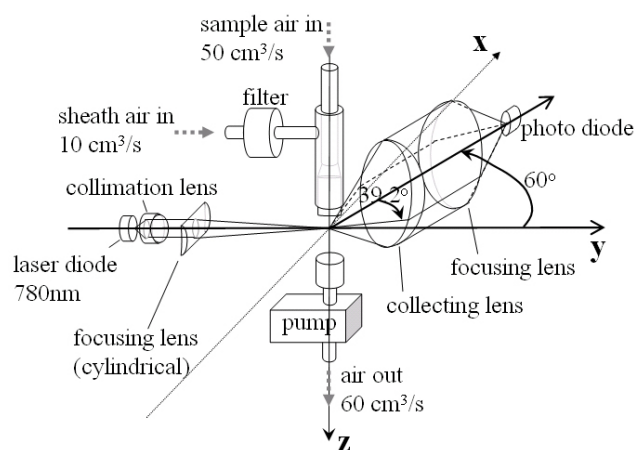
Fig. 1. Schematic diagram of OPC. Transmitted laser beams are linear-polarized parallel to the x-y plane. The photo diode is on the x-y plane.

Stratospheric Aerosol and Gas Experiment (SAGE II), Wang et al. (1996) showed the frequency of SVC occurrence can exceed 50% over the warm water pool. Winker and Trepte (1998) examined SVCs observed in the Lidar In-space Technology Experiment (LITE) mission and reported that the horizontal scale of the SVCs was approximately 500 km. The effects of SVCs have been studied by many researchers. Wang et al. (1996) also showed that SVCs significantly affect the radiation budget, and Eguchi and Shiotani (2004) reported that SVCs lead to the dehydration of air entering the stratosphere. Gettelman et al. (2004) reported on the basis of computations that water vapor is the most important contributor to the TTL radiation balance where the water vapor content is affected by the presence of SVCs. Therefore, SVCs are considered to play an important role in controlling radiation and water vapor content in the TTL. Historical and recent studies on SVCs are summarized in the work of Lynch et al. (2002, Chapter 12) and Hasebe et al. (2005).

Boehm and Verlinde (2000) was the first to report an analysis of SVCs on the basis of combined lidar and radiosonde data, and concluded that SVCs are generated by negative temperature anomalies induced by Kelvin waves. Comstock et al. (2002) analyzed the same data over 7 months, including the month analyzed by Boehm and Verlinde (2000), and determined that high cirrus with a cloud base of greater than 15 km does not coincide with negative temperature anomalies as often as found by Boehm and Verlinde (2000). Iwasaki et al. (2004) and Matsuura (2005) analyzed ship-borne lidar and radiosonde data and obtained similar findings to Comstock et al. (2002). To evaluate these studies, extensive observations and analyses of SVCs using lidar and radiosonde instruments have been performed by many researchers.

Jensen et al. (1996) and Jensen and Pfister (2004) investigated the SVC generation mechanism through calculations of cloud microphysics in the TTL using Lagrangian one-

dimensional models. Their results suggest that the injection of water vapor by deep convection is required to explain the observed humidity in the TTL.

To improve the numerical models of SVC generation and to validate computational results, observations of cloud condensation nuclei (CCN) and SVC particles are important. However, few studies have investigated aerosol and cloud particles at temperatures in the range of −80°C in the tropics. Peter et al. (2003) examined the microphysics of ultra-thin tropical tropopause clouds by airborne lidar observations and particle counter measurements over the Indian Ocean, and presented a summary of the cloud morphology. Kojima et al. (2004) reported the chemical components of aerosols in the TTL based on transmission electron microscopy (TEM) measurements. Both of these studies involved airborne measurements, which are expensive to conduct and are not suitable for measuring the vertical profiles of aerosol and cloud particles. In this study, a balloon-borne optical particle counter (OPC) is used to obtain more useful measurements, coupled with simultaneous lidar measurements. The measurement campaign was conducted from April to June 2003 in Thailand (17.2° N, 99.9° E).

The specifications of the OPCs and the lidar are described in Sect. 2. Our observational results are shown in Sect. 3 and discussed them in Sect. 4. Finally, we summarize the study in Sect. 5.

2 Instruments

2.1 Optical particle counter

The optical particle counter (OPC) employed in this study provides 8 channels of detection, corresponding to radii from 0.15 to 3.5 μm assuming spherical sulfuric acid particles, and counts particle number at each size. The data obtained are integrated number concentrations N (/m^3). Figure 1 shows a schematic diagram of the OPC instrument. Particles in the ambient air are guided by a pump through the beams of laser diodes transmitting at 780 nm. The detected light power $I_0 \Delta C_{sca}$ (W), where I_0 denotes the incident laser intensity (W/m^2) and ΔC_{sca} (m^2) is defined in Eq. (1), is detected by a photodiode via two lenses.

$$\Delta C_{sca} = \int_{\Delta\Omega} \frac{dC_{sca}}{d\Omega} d\Omega, \tag{1}$$

where Ω and $dC_{sca}/d\Omega$ denote the solid angle (str) and the differential scattering cross section of a particle (m^2/str), respectively, and the integral is implemented with scattering angle of 60° and half solid angle of 39.2°. The scattering at this angle is affected by less structural interference than other angles. The result, particle count value, is obtained from a look-up table of ΔC_{sca} and r. The table is pre-calculated by Mie theory assuming the particle whose refractive index is 1.4+i0 where it is corresponding to a sulfuric acid solution

Table 1. Specification of balloon-borne optical particle counter.

Dimension (L×W×H):	25×38×31 cm
Weight:	3.5 kg (including battery)
Light source:	Laser diode
wavelength	780 nm (70 mW of output)
Detection:	Lateral scattering light with a photodiode
Angle of collecting axis	60° from source light
Width of collecting area	39.2° of half solid angle
Sampling flow rate:	50 cm^3/s (at ground level condition)
Particle counting:	8 channel parallel counter *
Integrating duration:	16 s
Data transmission:	Narrow FM (model RS-01G: MEISEI Elec. Co. Ltd)
Carrier wave:	400 MHz (model RS-01G, MEISEI Elec. Co. Ltd)
Modulation:	FSK (Bell103 2025/2225 Hz)

* In the case of spherical sulfuric acid particles, each channel counts the numbers of particles with radii greater than 0.15, 0.25, 0.42, 0.66, 0.97, 1.73, 2.50, and 3.54 μm (see Appendix A and Table 3).

with 40 wt% concentration (Baumardner et al., 1996; Steele and Hamill, 1981). The measurement errors due to irregularities in particle shape are calculated by the finite-difference time-domain (FDTD) method (e.g., Yang and Liou, 1995) as discussed in Appendix A. The minimum detectable N and the vertical resolution are approximately $1.5 \times 10^4/\text{m}^3$ and 50 m in the TTL. The detailed OPC specifications are listed in Table 1 and presented in Hayashi et al. (1998).

Note that the integrated number concentration changes induced by impaction on a wall and inside heat of OPC are negligible for smaller than 5 μm in radius. This is because (1) the stokes number (Eqs. 14–11 in Pruppacher and Klett, 2003) in the OPC flow system is 1 for a particle with 5 μm in radius where a dimension of the stainless inlet tube is 4.5 mm in diameter and 5 cm in length and a flow rate of sample air is 3 m/s, and (2) shrink ratio of particle size is less than 0.01 for a particle with 0.5 μm in radius (details are not shown).

The all OPC are calibrated by using monodisperse polystyrene latex spherical particles (PSL) whose refractive index is $1.59+i0$. We compared detected light power by 7 different sizes of the PSL particles from 0.127 to 2.5 μm in radius and theoretical values calculated by the Mie theory, and checked the observational error of the OPCs is less than 5% in each size. Then each threshold of each channel is set to be ΔC_{sca} of the spherical particle whose radius and refractive index are 0.15, 0.25, 0.42, 0.66, 0.97, 1.7, 2.5, 3.5 μm and $1.40+i0$, respectively (see Appendix A, Fig. A1).

The size distribution dn/dr (number/μm/m^3) is derived by subtracting data on adjacent channels; e.g., dn/dr at 0.2 μm, from 0.15 μm and 0.25 μm channels, is calculated from the following equation.

$$\left.\frac{dn}{dr}\right|_{r=0.2\mu m} = \frac{N|_{r=0.25\mu m} - N|_{r=0.15\mu m}}{0.25 - 0.15}. \qquad (2)$$

As channel 8 of the OPC measures all particles larger than 3.5 μm radius, the maximum particle radius for the size dis-

tribution $dn/dr|_{r=3.5-5.2\,\mu m}$ is assumed to be 5.2 μm. Therefore, the accuracy of dn/dr for the largest particle size is not known.

Note that smaller particles ($<1\,\mu$m radius) are assumed as liquid particles, corresponding to the Junge layer, and particles detected on channel 8 are assumed to be ice particles, as explained in Appendix B. We do not assume that the other particles are either liquid or solid. Therefore, "particles" in this paper refer to both aerosols and cloud particles, as distinction between the two types is not possible with the present OPC. Consequently, in presenting OPC data, we have applied error bars to indicate this variation in size (see Appendix A).

2.2 Lidar

The lidar used in the present study is based on a Nd:YAG laser (wavelengths are 1064 nm and 532 nm) with both transmitted energy of 20 mJ per pulse at a pulse repetition frequency of 10 Hz. The lidar return signal is received by two photomultiplier tubes at 532 nm to determine the depolarization ratio and an avalanche photodiode at 1064 nm through a 20 cm telescope. The laser was configured to fire beams for 5 min then cool down for 10 min in order to prolong the life of the flashlamp that induces the laser pulse. Each datum was obtained as the average over 5 min. The vertical resolution of lidar measurements was set at 6 m. A range of temporal and vertical resolutions could be set on the laptop computer connected to the lidar instrument.

The lidar was able to detect backscattering coefficient by gas at altitudes of up to 14 km high on a clear day at 532 nm using the 5 min average over a length of 100 m, where the backscattering coefficient β (/m/str) is defined as Eq. (3).

$$\beta = \frac{1}{4\pi} \int C_{bk}(r) \frac{dn}{dr} dr, \qquad (3)$$

(a)

(b)
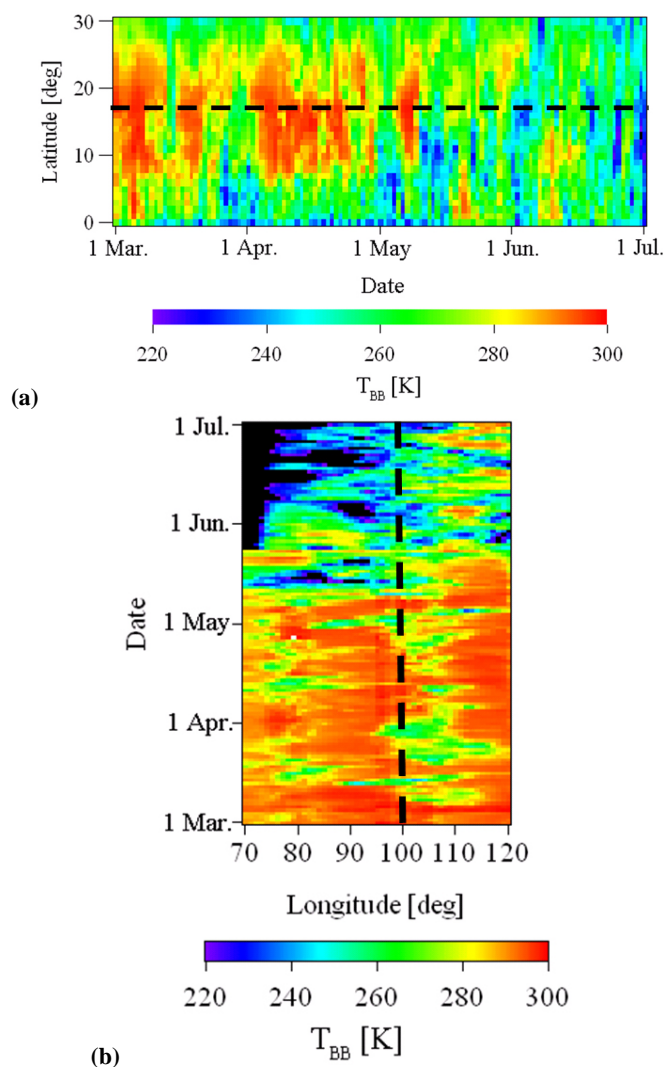
Fig. 2. Black body temperature (T_{BB}) measured with GMS and GOES. **(a)** Time-latitude and **(b)** time-longitude sections centered on the observation site (17.16±0.5° N, 99.87±0.5° E) from 0° N to 30° N and from 70° E to 120° E, respectively where dashed line denotes the site and bluer denotes deeper convection. The deep convection of the monsoon, whose horizontal scale in longitude is 1–2×10³ km, extended northward into the Sri Samrong from late in May.

where $C_{bk}(r)$ denotes the backscattering cross section (m²).The sensitivity of the instrument at 532 nm is therefore approximately 3×10^{-7}/m/str.

Due to noise at 1064 nm, we analyze backscattering coefficient at 532 nm ($\beta(532)$). To calibrate the data, the lidar return was fitted to $\beta(532)$ calculated from the pressure and temperature measured by the OPC at heights of 10 km to 13 km without cloud below. Hence, the calibration corrects the attenuation below 10 km. The depolarization ratio was also fitted to the values estimated by the OPC at a height of approximately 4 km.

3 Observations

3.1 Observational period and site

The observation period was from March to June in 2003. Lidar measurements were implemented throughout this period at Sri Samrong (17.16° N, 99.87° E) in Thailand. Radiosonde instruments were launched once a day adjacent to the lidar site. A total of 3 one-week intensive observation periods (IOPs) were performed from March to June. The OPC were launched in IOPs as listed in Table 2.

3.2 T_{BB}

Figure 2 shows (a) time-latitude and (b) time-longitude sections of T_{BB} (°K) centered on 17.16±0.5° N, 99.87±0.5° E from 0° N to 30° N and from 70° E to 120° E, respectively, where T_{BB} was measured with the geostational meteorological satellite (GMS) and the geostationary operational environmental satellite (GOES) since GMS was stopped the operation after 22 May 2003. Figure 2a shows that the deep convection (bluer T_{BB}) of the monsoon extended northward into the Sri Samrong from late in May, with Fig. 2b indicating the horizontal scale in longitude is 1–2×10³ km.

Of the 11 OPC launches, TTL clouds were detected on 6 occasions, among which 4 detections were from late in May. As the lifetime of TTL cloud is typically less than 1 day due to its terminal velocity (Iwasaki et al., 2004, Fig. 3), each OPC detected different clouds. Therefore, TTL clouds are observed frequently in the vicinity of deep convective systems.

3.3 Comparison of lidar and OPC data

Table 2 summaries the particle numbers and maximum β in the TTL cloud. Two simultaneous observations by lidar and OPC were conducted on 24 April and 29 May. Figure 3 shows the vertical integrated number concentration and temperature measured with OPC and the time-height section of lidar backscattering coefficient on (a, b) 24 April and (c, d) 29 May where black arrows in Figs. 3a, c and yellow arrows in Figs. 3b, d denote TTL cloud and the time that OPC existed in the TTL, respectively, where data of the channel 1 on 24 April is not shown due to noise (Fig. 3a) and lidar data are masked due to rain at 03:00–06:00 UT on 29 May (Fig. 3d). Table 2 shows cloud heights measured by lidar are hundreds of meters higher than those measured by the OPC, probably due to spatial variation in cloud height as the OPC moves tens kilometers from the launch site by wind. Note that this height difference is not due to the instrumental error because lidar measurements of cloud heights below 15 km are not always higher than those recorded by the OPC; e.g., Fig. 4 shows vertical profiles of backscattering coefficient and accumulated particle number measured on 26 March; the cloud heights of which integrated number concentration measured by OPC is the maximum are higher than the heights whose β
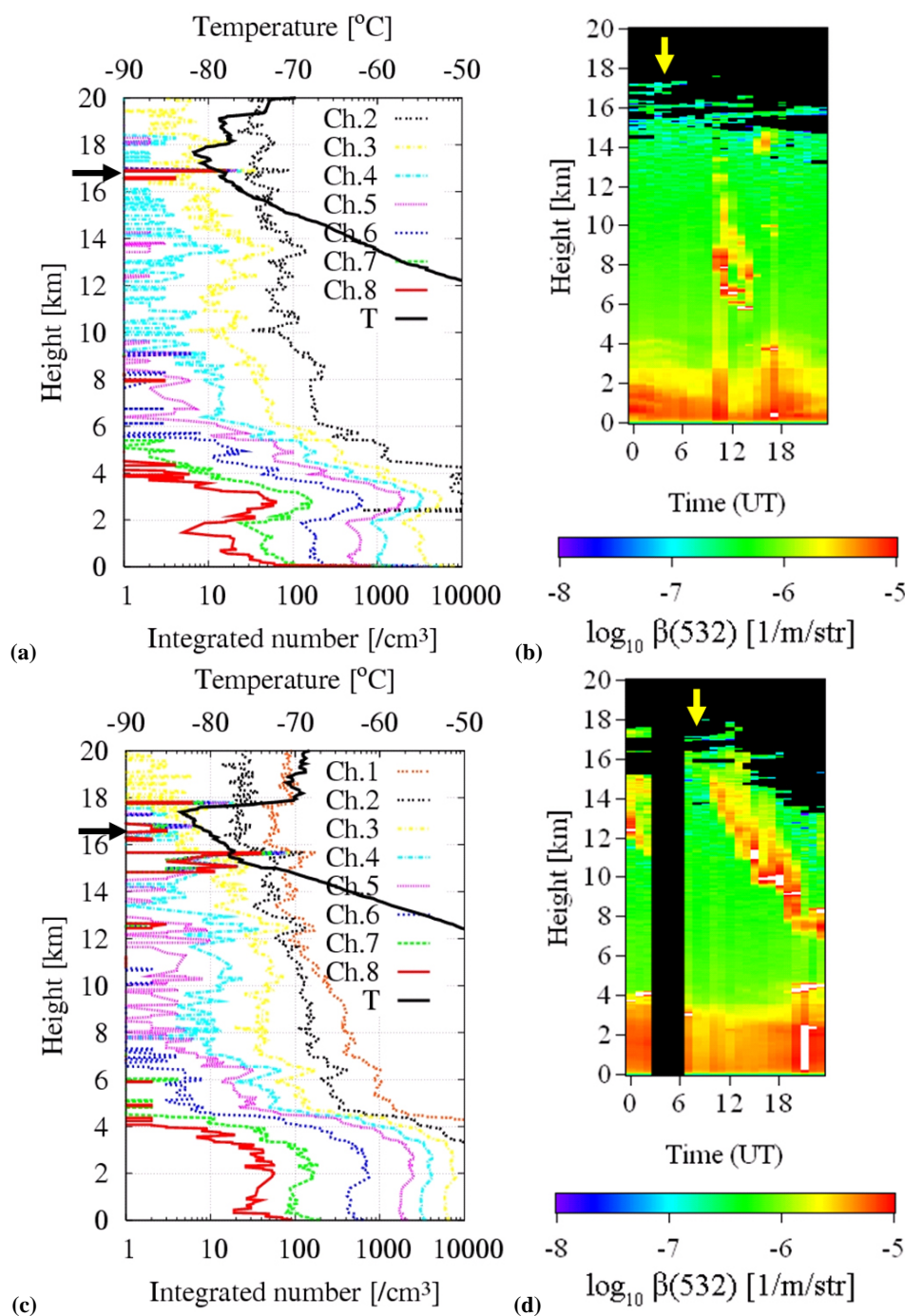
Fig. 3. **(a, c)** The vertical integrated number concentration and temperature measured with OPC and **(b, d)** time-height section of lidar backscattering coefficient on (a, b) 24 April and (c, d) 29 May where a black arrow in (a, c) denotes TTL cloud and yellow one in (b, d) denotes the time that OPC existed in the TTL. The lidar data are masked due to rain at 03:00–06:00 UT on 29 May (d).

measured by lidar is the maximum at around 6.5 km, which implies that there is no height bias between OPC and lidar. In addition, Fig. 5 of Peter et al. (2003) and Fig. 7 of Martucci et al. (2006) show an air-borne lidar measurement that the TTL cloud height was also different about hundreds meter within

tens km even though the cloud was geometrically thin cirrus. Therefore, TTL cloud height is not always horizontally uniform.

It is assumed for the present purposes that the cloud microphysics measured simultaneously by the lidar and OPC in the

Table 2. Particle numbers and $\beta_{MAX}(532)$ measured with the OPCs and the lidar in TTL.

	OPC	Lidar
Launched time (UT)	Number on channel 8 [/m^3] Height [km], Temperature [°C]	$\beta_{MAX}(532)$ [/m/str] Height [km]
06:46, 26 March	–	–
22:00, 26 March	–	–
03:50, 27 March	4.5×10^3/m^3 17.7 km, -77.7°C	–
06:14, 23 April	–	–
03:17, 24 April	3.2×10^4/m^3 16.9 km, -78.6°C	2.4×10^{-7}/m/str 17.1–17.3 km
18:23, 25 April	–	–
14:17, 26 April	–	–
06:59, 29 May	5.9×10^3/m^3 16.5–16.9 km, -80.0 to -82.0°C	4.0×10^{-7}/m/str 17.0–17.2 km
12:26, 30 May	4.2×10^5/m^3 16.8–18.3 km, -78.3 to -83.2°C	X
00:22, 1 June	6.3×10^4/m^3 16.1–16.3 km, -77.0 to -77.4°C	X
07:15, 4 June	6.5×10^4/m^3 16.6–17.3 km, -79.3 to -82.6°C	X

No entry indicates that no TTL cloud was detected. X denotes cases in which lidar observation in the TTL was not possible due to optically dense clouds below the TTL. $\beta_{MAX}(532)$ denotes the maximum β at 532 nm in TTL clouds and β is averaged for 1 h and 100 m.

TTL are the same; hence, the microphysical values presented below are estimates.

Because the cloud number concentration N_{cl} is given by the OPC for particle radii greater than 3.3 μm, and β is given by lidar, the mode radius r_g or standard deviation σ_g of the particle size distribution can be obtained assuming the size distribution of cloud particles to be log-normal as follows.

$$\frac{dn}{dr} = \frac{N_{cl}}{\sqrt{2\pi}\ln\sigma_g}\frac{1}{r}\exp\left[-\left(\frac{\ln r - \ln r_g}{\sqrt{2}\ln\sigma_g}\right)^2\right]. \qquad (4)$$

Mie theory (Bohren and Huffman, 1998) is applied for the analysis and the reason is as follows: It is impossible at present to calculate the backscattering cross section from an irregularly shaped particle with size parameter (=$2\pi r/\lambda$, radius r and wavelength λ) of greater than approximately 50 due to the limitations of computer power. Therefore, an approximation is required for the analysis. Iwasaki and Okamoto (2001) estimated backscattering on the basis of Kirchhoff's diffraction theory, and showed that the backscattering of 20 μm plate-like particles with horizontally random orientation is expected to be one order of magnitude larger than for spherical particles. However, as this orientation is rare, and randomly oriented particles produce similar signals as spheres.

Assuming σ_g of 1.6, the maximum r_g is estimated to be 3.6 μm for the TTL clouds detected on 24 April, and 11.2 μm for 29 May, where N_{cl} is 3.2×10^4 and 5.9×10^3/m^3, and

$\beta(532)$ is 2.4×10^{-7} and 4.0×10^{-7}/m/str in the TTL, respectively.

3.4 OPC results I: integrated number concentration

Figure 5 shows the averaged integrated number concentration $<N>$ obtained by OPC measurements. At first, we divided one OPC vertical number profile into the data at 10–15 km (a, b) and the height at which temperature is lower than -75°C, $H_{T<-75C}$, (c, d). We then divided the two profiles into the data with and without clouds. Therefore, e.g., 4 graphs are drawn from one launching on 1 June. -75°C is used as an empirical value with which to distinguish between TTL cloud and usual cirrus clouds, such as anvil clouds. This is because there appears to be no temperature and height threshold at which TTL cloud appears. For example, Table 12.1 in Lynch et al. (2002) shows that TTL cloud appears from -40°C to -90°C. However, this temperature is not applicable as it is not possible to distinguish between TTL and anvil clouds in the tropics.

The error bars at equivalent radius r_{eq} are calculated by the scattering of irregularly shaped particles and different refractive indices as explained in Appendix A and those at $<N>$ are the standard deviation of Poisson distribution.

Without clouds (Figs. 5a and c), $<N>$ decreases monotonically with regression lines of $1.7\times10^3 r^{-3.4}$/m^3 (10–15 km) and $5.1\times10^2 r^{-3.8}$/m^3 ($H_{T<-75C}$), where the radius r is in micrometers. On the other hand, $<N>$ with clouds

(b, d) also decreases, but it departs from the $<N>$ without clouds (a, c) at radii greater than approximately $0.8\,\mu m$, respectively; the regression lines are plotted to facilitate comparison in Figs. 5a, c and 5b, d. Therefore, the enhancement of integrated number is the common feature of a cloud at 10–15 km and $H_{T<-75C}$.

3.5 OPC results II: size distribution

Figure 6 is the same as Fig. 5 but the averaged particle size distributions dn/dr. The regressions line of dn/dr for the vertical size profile of background aerosols (Figs. 6a, c) are $8.2\times10^3 r^{-4.1}$ at 10–15 km high and $2.9\times10^3 r^{-4.7}/m^3$ at $H_{T<-75C}$, respectively. Aerosols in the TTL are known to form the Junge layer, primarily consisting of sulfuric acid and ammonium sulfate solution (e.g., Hobbs, 2000; Kojima et al., 2004, Table 2). dn/dr from 10 to 15 km high and that in TTL (Figs. 6b and d) show that most dn/dr for smaller particles decreases monotonically, with the regression lines fitting up to $2.0\,\mu m$ and $0.9\,\mu m$, respectively.

Of the 7 OPCs detected between 10 km and 15 km, only one (1 June) involved an enhancement from $0.9\,\mu m$, while no particles at $2.9\,\mu m$ were detected at 10–15 km on three occasions. Figure 6d shows 6 results for TTL clouds, of which 4 cases exhibit the enhancement from $0.9\,\mu m$ (24 April, 30 May, 1 June, 4 June) while Fig. 6b shows 1 case exhibits the enhancement at $1.3\,\mu m$ at 10–15 km high (29 May). Note that enhancements at $4.5\,\mu m$ in Figs. 6b and d are not reliable because the values of dn/dr at $4.5\,\mu m$ are not accurate (see Sect. 2.1). Therefore, the enhancement from $0.9\,\mu m$ is a typical feature of the TTL cloud.

3.6 OPC results III: ratio of standard deviations of count value to Poisson distribution

Figure 7 is a ratio of σ(counts) and σ(Poisson), where σ(counts) denotes standard deviation of particle count values N_{raw}, raw data of OPC, at each channel, and σ(Poisson) denotes that of the Poisson distribution, as defined in Eq. (5) in the case at $H_{T<-75C}$.

$$\sigma(counts) = \sqrt{\frac{1}{N}\sum_{T<-75}^{N}\left(N_{raw} - \langle N_{raw}\rangle|_{T<-75}\right)^2}.$$
$$\sigma(Poisson) = \sqrt{\langle N_{raw}\rangle|_{T<-75}} \qquad (5)$$

In this case, we calculate two ratios by using one OPC data at 10–15 km (a, c) and at $H_{T<-75C}$ (b, d), and classified the ratios when cloud exist (b, d) or not (a, c), respectively. Therefore, e.g., one profile is divided into 2 graphs on 1 June. This ratio becomes one for a vertically homogeneous cloud, and represents a useful indicator of the vertical homogeneity of the particle number.

Figure 7 shows that the ratio is lower in cases when no cloud was detected (a, c) than when cloud was present (b, d), respectively. Hence, the vertical profiles of background aerosols are relatively uniform. In addition, the average ratio
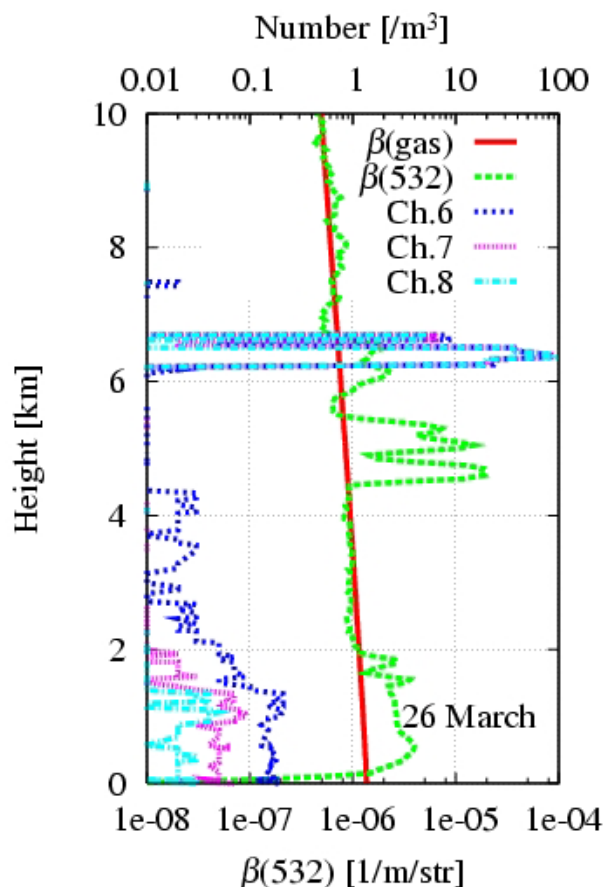
Fig. 4. Vertical profiles of backscattering coefficient, β (532) and β (gas), and integrated particle number, Ch.6, 7, and 8 of OPC, measured on 26 March. The cloud heights of which integrated number concentration is the maximum are higher than the heights whose β is the maximum at around 6.5 km; hence, cloud heights measured by lidar are not always higher than those by the OPC.

over the 10–15 km altitude (a, b) is greater than that in the TTL (c, d). This is because the variation of height is different, that is, 5 km depth in Figs. 7a, b and approximately 3 km depth in Figs. 7c, d, and because the ice nucleation in Fig. 7b is more active than that in Fig. 7d due to deep convection and higher temperature. In addition, there are peaks at around $0.8\,\mu m$ when the TTL clouds exist (d) while there is no peak at 10–15 km high (b); hence, the peak is also a typical feature of the TTL cloud.

4 Discussion

Figure 5 shows that cirrus clouds at 10–15 km were detected on 7 OPC launches, and in 6 cases TTL clouds were detected. Since smaller particles ($<1\,\mu m$ radius) are liquid particles, corresponding to the known Junge layer, while particles larger than $3\,\mu m$ in radius are ice particles (Appendix B), it is considered that liquid particles are frozen in
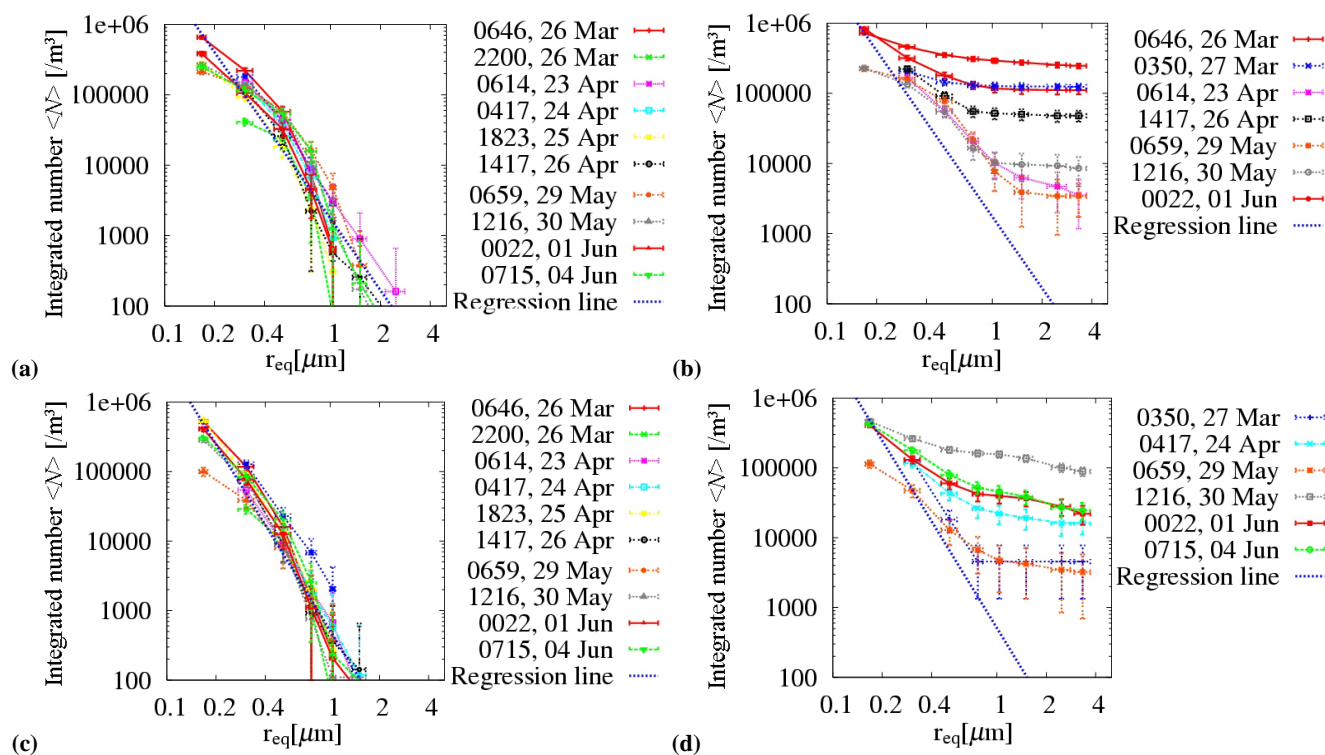
Fig. 5. Integrated number of particles **(a, b)** at 10–15 km and **(c, d)** at $H_{T<-75C}$ under conditions of (a, c) no cloud (background aerosols) and (b, d) cloud. Regression lines are $1.7 \times 10^3 r^{-3.4}$/m³ in (a, b), and $5.1 \times 10^2 r^{-3.8}$/m³ in (c, d). Integrated number with clouds (b, d) is departs from that without clouds (a, c) at approximately 0.8 μm or larger, and this is the common feature of a cloud at 10–15 km and $H_{T<-75C}$.

the intermediate size range. Hayashi et al. (1998) showed that enhancement in the integrated number of particles on the largest channel ($r > 1.8$ μm) indicates polar stratospheric clouds (PSCs) consisting of ice particles. By analogy with the PSC study, the results in Fig. 5 suggest that liquid particles tend to be frozen at approximately $r > 0.8$ μm above 10 km high, and smaller liquid particles in TTL cloud are enable to be frozen compared with those in PSC.

Figure 6 shows only once was an enhancement in the size distribution at 0.9 μm detected at 10–15 km, while in 4 cases the enhancement was observed in the TTL; hence this is a typical feature in TTL cloud. This result suggests that the speed of cloud growth below 15 km is much higher than that at $H_{T<-75C}$, and the transition from liquid to ice is less observable since the mixing ratio is higher at warmer temperatures. For example, the growth times of ice particles in the 0.1–3 μm size range at −60 and −80°C are 40 s and 13 min under a relative humidity with respect to ice (RHi) of 120% (see Appendix B). Once liquid particles are frozen, a gap forms in the size distribution due to the Bergeron-Findeisen process (e.g., Emanuel, 1994); This gap is observed at 1.9 or 2.9 μm on three launches at 10–15 km (27 March, 26 April, 29 May) and two launches in TTL (27 March, 24 April).

Figure 7 shows the ratio of σ(counts) to σ(Poisson) for ice clouds is different from that in cloud-free cases where the ratio reflects the vertical homogeneity of the particle number concentration. Thus it is a good indicator of the presence of ice particles. In addition, this ratio has a peak at around 0.8 μm when the TTL clouds are present (Fig. 7d), but not at heights of 10–15 km (Fig. 7b). This characteristic is thus a typical feature of the TTL cloud. The non-uniformity implies that particles in this size range are actively frozen, so that the timing of freezing may vary with height in the TTL.

5 Summary

A total of 11 OPC launches were conducted in Thailand from May to June 2003. On 6 occasions, cirrus clouds were detected in the tropical tropopause layer, 4 of which were detected around deep convection; TTL clouds were observed frequently in the vicinity of deep convective systems. The particle sizes measured by the OPC were re-calculated by the FDTD method in order to account for observation error induced by irregularly shaped particles and different refractive indexes. Lidar observations were conducted simultaneously, and comparison of the lidar cloud heights with
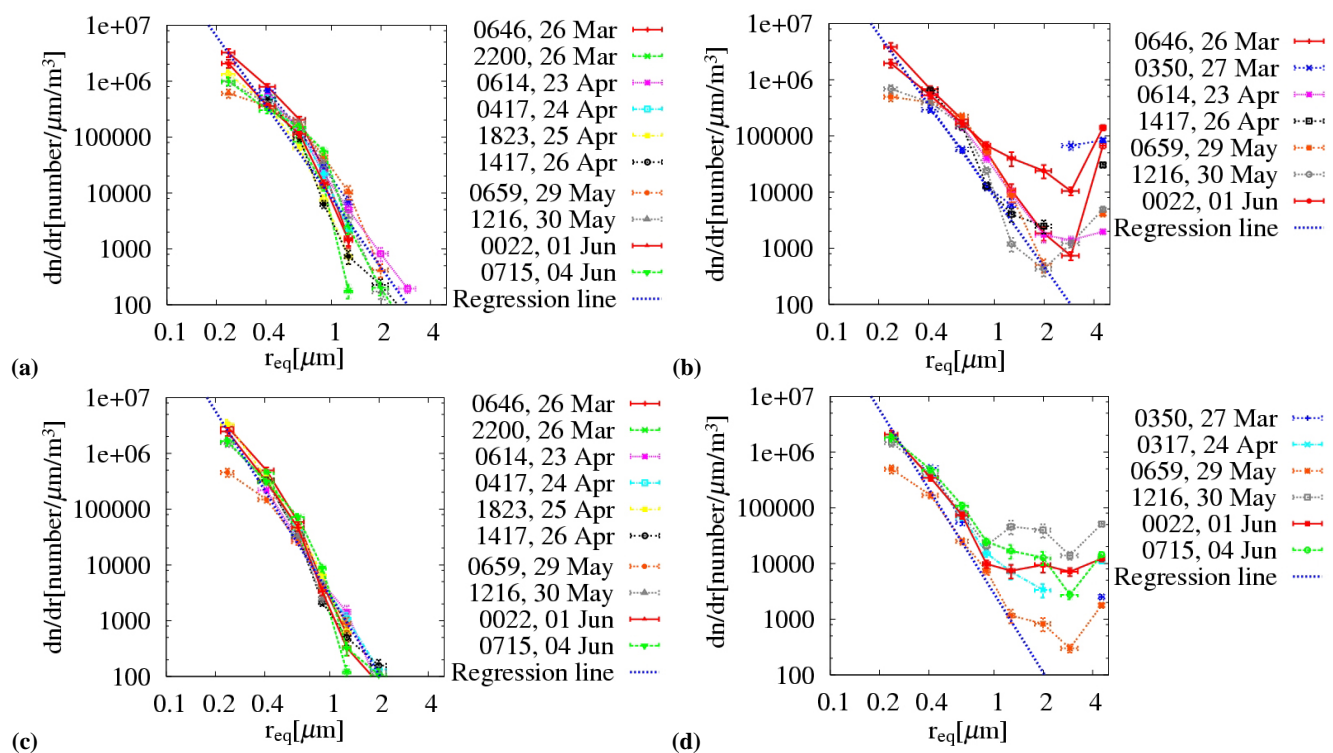
Fig. 6. The same as Fig. 5 but averaged particle size distributions. Regression lines in **(a, b)** and **(c, d)** are $8.2 \times 10^3 r^{-4.1}$ and $2.9 \times 10^3 r^{-4.7}/m^3$, respectively. These figures show the enhancement at $0.9\,\mu m$ compared with aerosol size distribution is a typical feature of the TTL cloud.

the OPC results indicates that the TTL cloud heights varies by several hundred meters over distances of tens kilometers; hence the height is not horizontally uniform, despite the huge horizontal scale ($\sim$500 km; Winker and Trepte, 1998) and geometrical thinness of such clouds. The mode radius of particles in clouds was estimated to be less than approximately $10\,\mu m$ on the basis of both OPC and lidar data. For example, the maximum mode radii for clouds detected on 24 April and 29 May are estimated to be $3.6\,\mu m$ and $11.2\,\mu m$ assuming a standard deviation as $1.6\,\mu m$.

Enhancements in the integrated number concentration greater than around $0.8\,\mu m$ are common feature of cloud above 10 km high, while an enhancements in the particle size distribution at $0.9\,\mu m$ and the peak of $\sigma(counts)/\sigma(Poisson)$ at around $0.8\,\mu m$ are typical feature in TTL cloud.

As these features are common and particular to cirrus clouds, the characteristic size distributions for particle radii of 0.5–$3.0\,\mu m$ obtained in this study should also be seen in ice nucleation studies and computer simulations of TTL clouds. The present study thus yields some interesting results pertaining to ice nucleation, and demonstrates that OPCs are effective for observing both aerosols and the generation mechanism of cirrus clouds in the TTL. A comparison of OPC data with a model which includes particle size distri-

bution will be presented as part of future validation of the present results.

Appendix A

Size error in OPC data

The OPC counts particle number at each size when ΔC_{sca} measured by a photo diode (see Fig. 1) is greater than each threshold as shown in Fig. A1, where ΔC_{sca} is proportional to detected light power and calculated by Mie theory and the FDTD method (e.g., Yang and Liou 1995); e.g., channel 1 counts particles when ΔC_{sca} is greater than $0.002\,\mu m^2$ and channel 2 counts when it is greater than $0.004\,\mu m^2$. The size error introduced by the various irregularly shaped particles and the difference in refractive index is estimated as follows.

Four shapes of particles are examined. In Fig. A1, "Sphere" denotes spherical particles with refractive indexes of $1.4+i0$ and $1.3+i0$, corresponding to sulfuric acid solution with 40 wt% concentration (Baumardner et al., 1996; Steele and Hamill, 1981) and water ice (Warren, 1984), respectively. Model A denotes an 8-hexagonal aggregate defined in Yang and Liou (1998), model B is the same but with all distances of barycenters half that of model A, as defined
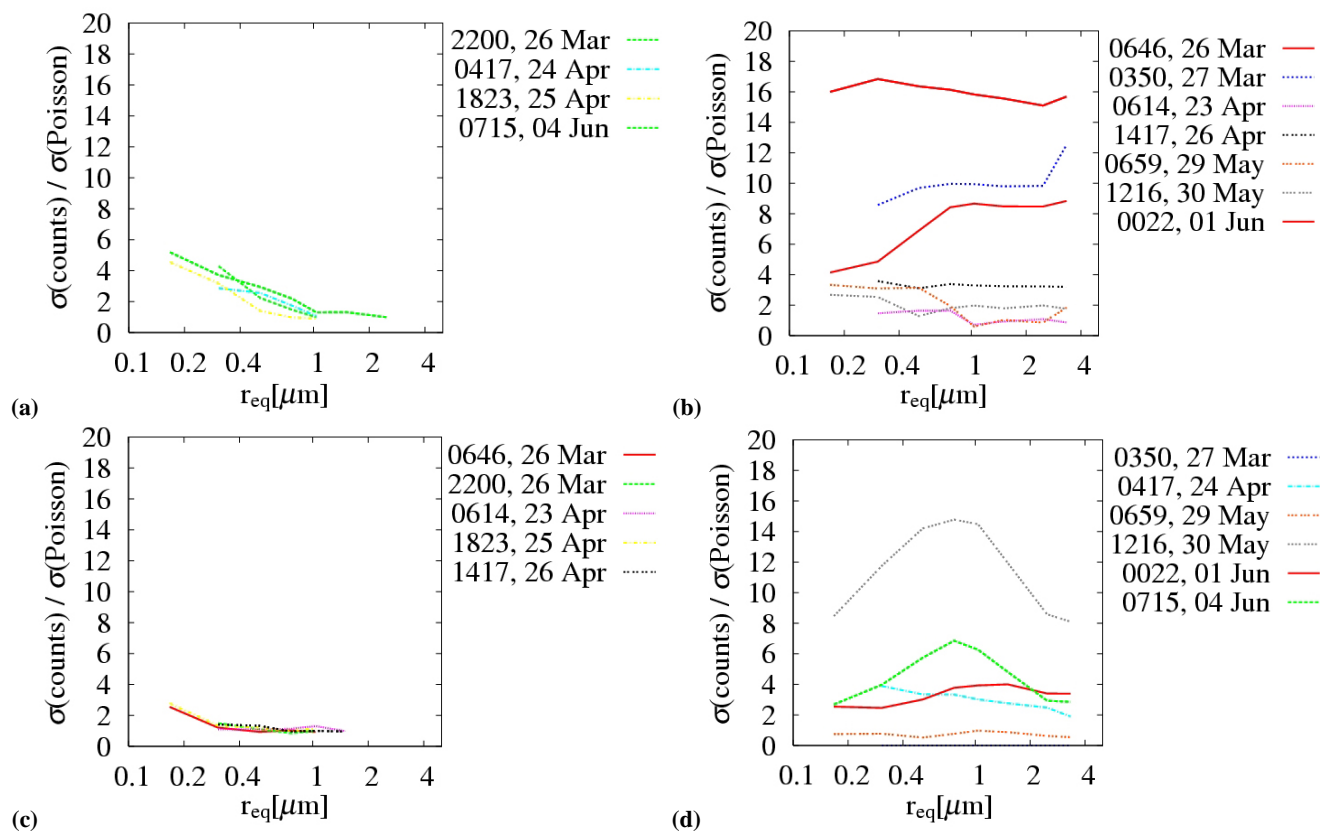
Fig. 7. Ratio of standard deviation of counts (raw data) to that of the Poisson distribution of average counts **(a, b)** at 10–15 km and **(c, d)** at $H_{T < -75C}$ under conditions of (a, c) no cloud (background aerosols) and (b, d) cloud. Figures show the vertical profiles of background aerosols (a, c) are relatively uniform and peaks at around $0.8\,\mu$m in the TTL clouds (d) is a typical feature of the TTL cloud.

Table A1. Radius thresholds in each OPC channel.

	H_2SO_4	Water ice	Model A	Model B	Model C	Average	σ
Ch.1	0.15	0.17	0.18	0.17	0.17	0.17	0.01
Ch.2	0.25	0.30	0.36	0.31	0.31	0.31	0.03
Ch.3	0.42	0.51	0.60	0.52	0.51	0.51	0.06
Ch.4	0.66	0.81	0.80	0.78	0.77	0.76	0.06
Ch.5	0.97	1.08	1.01	1.04	1.08	1.03	0.04
Ch.6	1.73	1.60	1.34	1.39	1.46	1.51	0.15
Ch.7	2.50	2.99	1.98	2.35	2.58	2.48	0.33
Ch.8	3.54	3.71	2.65	3.22	3.54	3.33	0.37

Each channel counts particles whose radius is greater than numbers described in the table (see Appendix A). Average and σ denote average and standard deviation from H_2SO_4 solution to model C.

in Ishimoto and Kobayashi (2006), and model C denotes a hexagonal column with aspect ratio of 1.7, where the aspect ratio is defined as $2R/L$ with R and L being the lengths of one side of the hexagon and the column. Each irregularly shaped particle is randomly oriented and the refractive index is set to that of water ice.

Ishimoto and Kobayashi (2006) showed that scattering by model A is similar to the average scattering by individual hexagonal columns of the aggregate, while scattering by model B contains lots of interference of scattering by 8 hexagonal columns. That is, models A and B not only show the scattering by themselves but also represent the average scattering related to variously shaped hexagonal columns (model A) and complex-shaped particles (model B).
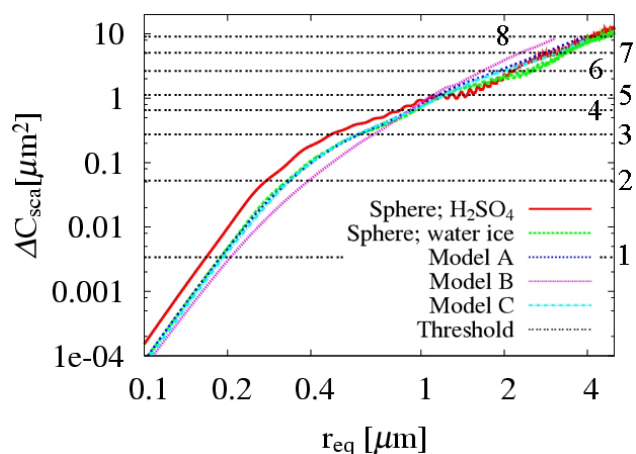
Fig. A1. Radius threshold in OPC. r_{eq} denotes the equivalent radius defined as $(3V/4\pi)^{1/3}$ where V is particle volume. ΔC_{sca} is proportional to detected light power (Eq. 1). Each curve is calculated by Mie theory and the FDTD method. OPC counts particle number at each size (channel) when detected ΔC_{sca} is greater than each threshold, where channel numbers are shown in right hand side; e.g., channel 1 counts a particle when ΔC_{sca} is greater than $0.002\,\mu m^2$.

To obtain modified r and the error bars in r, we average radius at each channel and calculate the standard deviations as summarized in Table 3. Moreover, since there are error bars in each radius, dn/dr also has error bars. To determine modified dn/dr and its error bar, we average each dn/dr and the standard deviations.

Appendix B

Growth rates of liquid and ice

The liquid and ice particle growth rates are calculated by the following equations, where r_w and r_i denote the radii of liquid and ice particles and t denotes time. All symbols are the same as those described in the Appendix of Spice et al. (1999).

$$\frac{dr_w}{dt} = \frac{1}{\rho_w r_w}\left(\sigma_w - \frac{b}{Tr_w} + \frac{cm_s}{r_w^3}\right)$$
$$\left[\frac{RT}{e_{s,w}D'_a M_w} + \frac{L_v}{K'_a T}\left(\frac{L_v M_w}{RT} - 1\right)\right]^{-1},$$

$$\frac{dr_i}{dt} = \frac{\sigma_i}{\rho_i r_i}\left[\frac{RT}{e_{s,i}D'_a M_w} + \frac{L_v}{K'_a T}\left(\frac{L_v M_w}{RT} - 1\right)\right]^{-1} \quad \text{(B1)}$$

Figure B1 shows the growth rate for sulfuric acid solution (liquid) and water ice particles of radius 0.1–3 μm at −80°C, where we assume the particle phase (liquid or ice) does not change. The molalities (number of moles of dissociated solute per unit mass of solvent) of sulfuric acid solution (liquid)
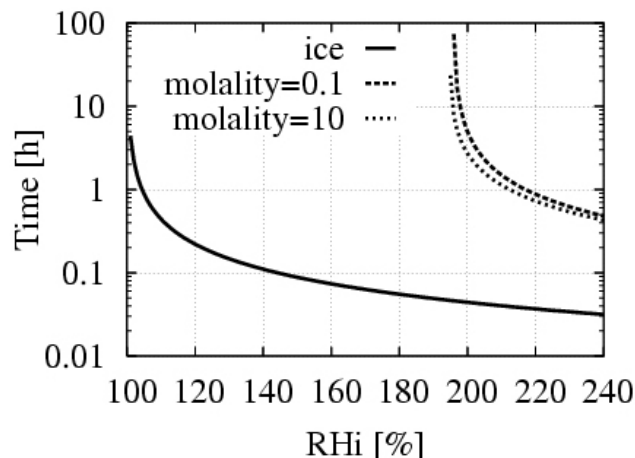
Fig. B1. Growth time for particles of radii 0.1–3 μm at −80°C where RHi and ambient temperature are assumed to be constant. The dashed curves denote sulfuric acid solution (liquid) whose molalities are 0.1 and 10, respectively, and the solid one denotes water ice. The graphs show liquid particles of the Junge layer cannot grow up to 3 μm without freezing since the condition of RHi>195 % is not realistic; hence, particles with 3 μm must be ice particles.

are 0.1 and 10, respectively. Because RHi and the ambient temperature are assumed to be constants, the graph shows the fastest growing rates. From Fig. B1, liquid particles can grow when RHi is greater than 195%, since the relative humidity with respect to water RHw is lower than RHi. The results for $(NH_4)_2SO_4$ solution also show similar results (data not shown). However, the value is not realistic (e.g., Jensen et al., 2001, Fig. 5). Hence, liquid particles of the Junge layer, cannot grow up to 3 μm without freezing, indicating that such large particles must be ice particles.

References

Baumgardner, D., Dye, J. E., Gandrud, B., Barr, K., Kelly, K., and Chan, K. R.: Refractive indices of aerosols in the upper troposphere and lower stratosphere, Geophys. Res. Lett., 23, 749–752, 1996.

Boehm, M. T. and Verlinde, J.: Stratospheric influence on upper tropospheric tropical cirrus, Geophys. Res. Lett., 27, 3209–3212, 2000.

Bohren, C. F. and Huffman, D. R.: Absorption and scattering of light by small particles, Wiley-Interscience, 530 pp., 1998.

Comstock, J. M., Ackerman, T., and Mace, G. G.: Ground-based lidar and radar remote sensing of tropical cirrus clouds at Nauru Island: Cloud statistics and radiative impacts, J. Geophys. Res., 107(D23), 4714, doi:10.1029/2002JD002203, 2002.

Eguchi, N. and Shiotani, M.: Intraseasonal variations of water vapor and cirrus clouds in the tropical upper troposphere, J. Geophys. Res., 109, D12106, doi:10.1029/2003JD004314, 2004.

Emanuel, K. A.: Atmospheric Convection, Oxford Univ. Press, New York, 1994.

Gettelman, A., Forster, P. M. de F., Fujiwara, M., Fu, Q., Vomel, H., Gohar, L. K., Johanson, C., and Ammerman, M.: Radiation balance of the tropical tropopause layer, J. Geophys. Res., 109, D07103, doi:10.1029/2003JD004190, 2004.

Hasebe, F., Shiotani, M., Fujiwara, M., Dunkerton, T. J., Folkins, I., Fortuin, P., Gettelman, A., Hashiguchi, N. O., Iwasaki, S., Kasai, Y., Nishi, N., Niwano, M., Oltmans, S., Poveda, L., Randel, W., Rosenlof, K., Tsushima, Y., Vömel, H., and Yamazaki, K.: Report of the 2nd International SOWER Meeting, SPARC Newsletter, 24, 21–27, 2005.

Hayashi, M., Iwasaka, Y., Watanabe, M., Shibata, T., Fujiwara, M., Adachi, H., Sakai, T., Nagatani, M., Gernandt, G., Neuber, R., and Tsuchiya, M.: Size and number concentration of liquid PSCs: Balloon-borne measurements at Ny-Alesund, Norway in winter of 1994/95, J. Meteorol. Soc. Japan, 76, 549–560, 1998.

Highwood, E. J. and Hoskins, B. J.: The tropical tropopause, Q. J. Roy. Meteor. Soc., 124, 1579–1604, 1998.

Hobbs, P. V.: Introduction to Atmospheric Chemistry, Cambridge Univ. Press, Cambridge, p. 179, 2000.

Ishimoto, H. and Kobayashi, T.: Effect of minor deformation for the light scattering of ice and aerosol particles, Proc. SPIE, 6408, 64081B, 2006.

Iwasaki, S. and Okamoto, H.: Analysis of the enhancement of backscattering by nonspherical particles with flat surfaces, Appl. Opt., 40, 6121–6129, 2001.

Iwasaki, S., Tsushima, Y., Shirooka, R., Katsumata, M., Yoneyama, K., Matsui, I., Shimizu, A., Sugimoto, N., Kamei, A., Kuroiwa, H., Kumagai, H., and Okamoto, H.: Subvisual cirrus cloud observations using a 1064-nm lidar, a 95 GHz cloud radar, and radiosondes in the warm pool region, Geophys. Res. Lett., 31, L09103, doi:10.1029/2003GL019377, 2004.

Jensen, E. J., Toon, O. B., Selkirk, H. B., Spinhirne, J. D., and Schoeberl, M. R.: On the formation and persistence of subvisual cirrus clouds near the tropical tropopause, J. Geophys. Res., 101, 21 361–21 375, 1996.

Jensen, E. J., Pfister, L., Ackerman, A. S., and Tabazadeh, A.: A conceptual model of the dehydration of air due to free-drying by optically thin, laminar cirrus rising slowly across the tropical tropopause, J. Geophys. Res., 106, 17 237–17 252, 2001.

Jensen, E. J. and Pfister, L.: Transport and freeze-drying in the tropical tropopause layer, J. Geophys. Res., 109, D02207, doi:10.1029/2003JD004022, 2004.

Kojima, T., Buseck, P. R., Wilson, J. C., Reeves, J. M., and Mahoney, M. J.: Aerosol particles from tropical convective systems: Cloud tops and cirrus anvils, J. Geophys. Res., 109, D12201, doi:10.1029/2003JD004504, 2004.

Lynch D. K., Sassen, K., Starr, D. O'C., and Stephens, G.: Cirrus, Oxford University Press, New York, 2002.

Martucci, G., Matthey, R., Mitev, V., Fix, A., and Kiemle, C.: Detection of ultra-thin tropical cirrus during TROCCINOX – A case study performed by two airborne lidars, Proc. of 23rd International laser radar conference, 585–588, 2006.

Matsuura, H.: A study on the cirrus variations near the tropical tropopause layer (TTL) by lidar measurement, M.S. thesis, Kyoto Univ., Japan, 31 March (in Japanese), 2005.

Peter, Th., Luo, B. P., Wirth, M., Kiemle, C., Flentje, H., Yushkov, V. A., Khattatov, V., Rudakov, V., Thomas, A., Borrmann, S., Toci, G., Mazzinghi, P., Beuermann, J., Schiller, C., Cairo, F., Donfrancesco, G. Di, Adriani, A., Volk, C. M., Strom, J., Noone, K., Mitev, V., MacKenzie, R. A., Carslaw, K. S., Trautmann, T., Santacesaria, V., and Stefanutti, L.: Ultrathin Tropical Tropopause Clouds (UTTCs): I. Cloud morphology and occurrence, Atmos. Chem. Phys., 3, 1083–1091, 2003, http://www.atmos-chem-phys.net/3/1083/2003/.

Pruppacher, H. R. and Klett, J. D.: Microphysics of Clouds and Precipitation, 2nd edition, Kluwer Academic Publishers, 2003.

Sassen, K. and Cho, B. S.: Subvisible-thin cirrus lidar dataset for satellite verification and climatological research, J. Appl. Meteorol., 31, 1275–1285, 1992.

Spice, A., Johnson, D. W., Brown, P. R. A., Darlison, A. G., and Saunders, C. P. R.: Primary ice nucleation in orographic cirrus cloud: A numerical simulation of the microphysics, Q. J. Roy. Meteor. Soc., 125, 1637–1667, 1999.

Steele, H. M. and Hamill, P.: Effects of temperature and humidity on the growth and optical properties of sulfuric acid-water droplets in the stratosphere, J. Aerosol Sci., 12, 517–528., 1981.

Yang, P. and Liou, K. N.: Light scattering by hexagonal crystals: Comparison of finite difference time domain method, J. Opt. Soc. Am., 12, 162–176, 1995.

Yang, P. and Liou, K. N.: Single-scattering properties of complex ice crystals in terrestrial atmosphere, Contr. Atmos. Phys., 71, 223–248, 1998.

Wang, P. H., Minnis, P., McCormick, M. P., Kent, G. S., and Skeens, K. M.: A 6-year climatology of cloud occurrence frequency from stratospheric aerosol and gas experiment II observations (1985–1990), J. Geophys. Res., 101, 29 407–29 430, 1996.

Warren, S. G.: Optical constants of ice from the ultraviolet to the microwave. Appl. Opt., 23, 1206–1225, 1984.

Winker, D. M. and Trepte, C. R.: Laminar cirrus observed near the tropical tropopause by LITE, Geophys. Res. Lett., 25, 3351–3354, 1998.